IN-SITU OPTIMIZED PWAS PHASED ARRAYS FOR LAMB WAVE STRUCTURAL HEALTH MONITORING

Lingyu Yu and Victor Giurgiutiu

IN-SITU OPTIMIZED PWAS PHASED ARRAYS FOR LAMB WAVE STRUCTURAL HEALTH MONITORING

LINGYU YU AND VICTOR GIURGIUTIU

The use of piezoelectric wafer active sensors (PWAS) phased arrays for Lamb wave damage detection in thin-wall structures is presented. The PWAS capability to tune into specific Lamb-wave modes (which is an enabling factor for our approach) is first reviewed. Then, a generic beamforming formulation that does not require the conventional parallel-ray approximation is developed for PWAS phased arrays in connection with the delay-and-sum beamforming principles. This generic formulation is applied to a 1-D linear PWAS phased array. Particularly, 1-D PWAS array beamforming reduces to the simplified parallel ray algorithm when the parallel ray approximation is invoked. The embedded ultrasonic structural radar (EUSR) algorithm is presented. A couple of simple experiments are used to show that the linear EUSR PWAS phased array system can successfully detect cracks in large aluminum thin plates.

To improve the EUSR image quality, advanced signal processing is studied for possible integration into the EUSR system. The approaches include Hilbert transform for envelope detection, thresholding techniques for removing background noise, discrete wavelet transform for denoising, continuous wavelet transform for single frequency component extraction, and cross-correlation for time-of-flight detection.

The optimization of linear PWAS arrays is studied next. First we consider the effect of several parameters affecting the phased-array beamforming: (1) number of elements M; (2) elementary spacing d; (3) steering angle ϕ_0; (4) location of the target r. Second, we examine the so-called nonuniform PWAS arrays which are generated by assigning different excitation weights to each of the array elements. The design of two nonuniform linear PWAS arrays, the binomial array and the Dolph–Chebyshev array, is presented. Significant improvement of the EUSR image is observed when using these nonuniform arrays.

1. Introduction

The current use of nondestructive evaluation (NDE) technologies is limited by the fact that the NDE inspection can be carried out only if the area to be inspected is accessible. In most cases, this can be achieved only during maintenance checks. For economic reasons, more frequent inspections or even continuous monitoring are not feasible with the existing NDE techniques [Beral and Speckmann 2003]. One method of conducting in-service monitoring of structural hot spots is through structural health monitoring (SHM) using guided waves and in-situ sensors. Guided waves can travel large distance with very little amplitude loss and inspect large area from a single transducer position [Rose 1995; 1999; 2001]. In-situ sensors, if sufficiently light and reliable, would offer on-demand structural interrogation capabilities.

1.1. *Motivation.* Traditionally, guided waves are generated by ultrasonic transducers that obliquely impinge onto a thin-wall structure. However, such ultrasonic transducers are unsuitable for in-situ SHM due to their cost, weight, and size. They cannot be attached in large numbers onto a structure without incurring important cost and weight penalties. The advent of commercially-available low-cost piezoelectric wafers has opened new opportunities for ultrasonic testing. Piezoelectric wafer active sensors (PWAS) are inexpensive lightweight unobtrusive transducers, which are well suited for SHM applications. These devices can be permanently attached to the structures for the generation and detection of guided waves [Giurgiutiu and Zagrai 2000]. Typical PWAS weigh 68 mg, are 0.2 mm thick, and cost less than US$10.

The advantages of using a phased array of transducers for ultrasonic testing are multiple [Moles et al. 2005]. Ultrasonic phased arrays use ultrasonic elements and electronic time delays to create wave beams by constructive wave interference. Rather than using a single transducer, the phased array utilizes a group of transducers located at distinct spatial locations. By sequentially firing the individual elements of an array at slightly different times, the ultrasonic wave front can be focused or steered in specific directions [Krautkramer and Krautkramer 1990]. The relative amplitudes of the signals radiated by the individual array elements determine the effective radiation pattern of the array. If the amplitude at a certain distance is the same for all directions, the wave field of the ultrasonic element is called omnidirectional. An array constructed of such elements, will have an effective radiation pattern that is uniquely determined by the beam steering algorithm alone. Inspection of a wide area can be achieved from a single location by electronically sweeping and/or refocusing the wave beam without physically manipulating the transducer. The backscattered ultrasonic signals received and stored in the computer can be numerically analyzed and mapped into an inspection image.

Current ultrasonic phased array technology employs pressure waves generated by ultrasonic transducers through normal impingement on the structural surface. Such phased arrays have shown clear advantages in the inspection of very thick specimens and in the sidewise inspection of thick slabs, where electronic beam scanning and focusing have produced significant improvements in the inspection efficiency. However, they cannot be efficiently used in thin-wall structures because of the small relative thickness of such structures. New transducers are therefore needed for efficient Lamb wave SHM using phased array technology.

PWAS phased arrays are capable of in-situ scanning of a large structural area using guided waves but without the need for actual physical scanning being performed. This advantage steers from the capability of PWAS phased array to see large areas from a single location [Giurgiutiu and Bao 2002]. A permanently mounted array of unobtrusive PWAS transducers was shown to map an entire half-plate and detect a small crack using the *embedded ultrasonics structural radar* (EUSR) methodology [Giurgiutiu et al. 2006]. The EUSR image resembles the C-scan of conventional ultrasonic surface scanning but without the need for actual physical motion of the transducer over the structural surface. Building onto these earlier results, this paper presents the results of a sustained effort to improve the EUSR-PWAS phased array concept through a generic phased-array formulation and the use of advanced signal processing methods. Phased-array design optimization is also discussed for better wave beam steering. This effort has resulted in increased detection capability, refined detection resolution, and extended detection range [Giurgiutiu and Yu 2006].

1.2. *Background.* The PWAS phased array technique is based on two important concepts: the use of PWAS for Lamb wave generation and detection, and the tuning between Lamb waves and PWAS that permits the transmission and reception of selective Lamb-wave modes, as appropriate for phased-array implementation. These concepts are briefly reviewed in this section.

PWAS coupled Lamb waves. When guided waves travel between two parallel surfaces which are sufficiently close, for example, a plate having a thickness of the order of a wavelength or so, they are called Lamb waves [Viktorov 1967]. In our work, Lamb waves were excited and detected using PWAS. PWAS operates on the piezoelectric principle that couples the electrical and mechanical variables in the material

$$S_{ij} = s^E_{ijkl}T_{kl} + d_{kij}E_k, \qquad D_j = d_{jkl}T_{kl} + \varepsilon^T_{jk}E_k,$$

where s^E_{ijkl} is the mechanical compliance of the material measured at zero electric field ($E = 0$), ε^T_{jk} is the dielectric permittivity measured at zero mechanical stress ($T = 0$), and d_{kij} represents the piezoelectric coupling effect. In Lamb wave application, PWAS couple their in-plane motion with the Lamb wave particle motion on the material surface. As an active sensor, PWAS can be used as transmitters and receivers to excite and detect Lamb waves. A surface mounted PWAS will couple with both the symmetric Lamb wave modes (S0, S1, S2, ...) and the antisymmetric Lamb wave modes (A0, A1, A2, ...). Figure 1 illustrates PWAS interaction with the S0 and A0 Lamb wave modes. Similarly to conventional
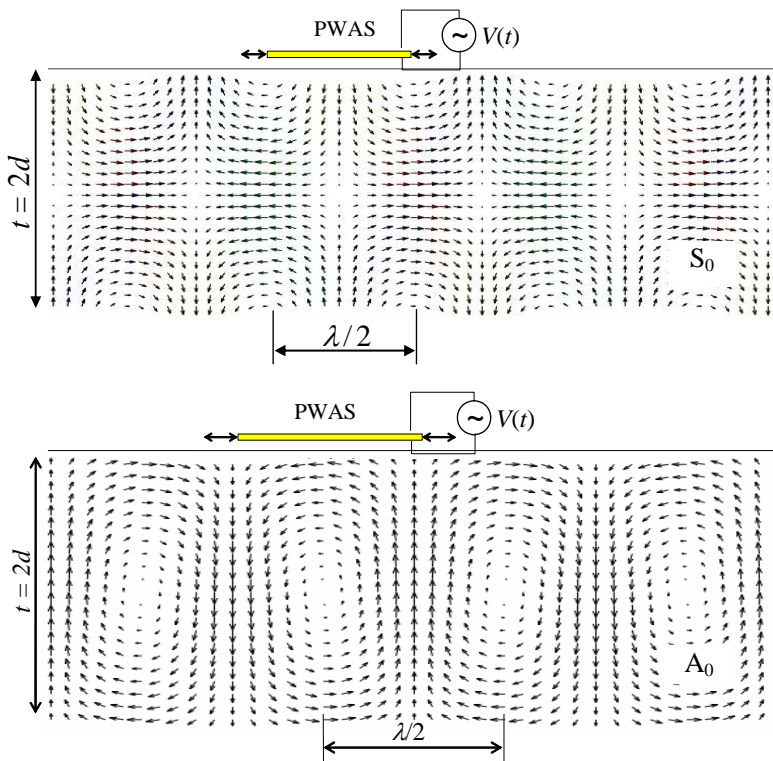

Figure 1. PWAS interaction with Lamb modes: top, symmetric mode S0; bottom, antisymmetric mode A0 [Giurgiutiu 2005].

ultrasonic transducers, PWAS can be used in pitch-catch, pulse-echo, phased array, etc. An extensive description of the use of PWAS for SHM can be found in [Giurgiutiu et al. 2006].

Lamb wave mode selection through PWAS tuning. Lamb waves are dispersive, that is, their phase velocity varies with the frequency, f, and the thickness of the material, $2d$. In addition, for any given frequency, at least two modes are present. The simultaneous presence of two or more Lamb wave modes complicates the use of Lamb waves for detecting structural damage. Besides, certain damage is more detectable with certain Lamb wave modes. In particular, the S0 wave mode is better for the detection of through-the-thickness cracks and A0 mode is better for corrosion and disbonding. For PWAS phased array application, it is better to selectively excite low-dispersion Lamb wave modes, such as S0 at low fd value. Given the PWAS length $2a$, wall thickness $2d$, and material properties μ and λ, it is possible to find tuning frequencies at which only one mode is excited; see [Giurgiutiu 2005]. A plane-strain analysis of the PWAS-structure interaction using the space-domain Fourier analysis was developed in the same paper to illustrate the principle of PWAS Lamb-wave mode tuning and open a path for a more comprehensive analysis. The analysis yielded the forward wave solution in the form

$$\varepsilon_x(x,t) = -j\frac{a\tau_0}{\mu}\sum_{\xi^S}\sin\xi^S a\frac{N_S(\xi^S)}{D_S'(\xi^S)}e^{j(\xi^S x-\omega t)}d\xi - j\frac{a\tau_0}{\mu}\sum_{\xi^A}\sin\xi^A a\frac{N_A(\xi^A)}{D_A'(\xi^A)}e^{j(\xi^A x-\omega t)}d\xi, \quad (1)$$

where τ_0 is the interfacial shear stress and ξ^S, ξ^A are the symmetric and antisymmetric wave numbers. The expressions for N_S, D_S, N_A, D_A are detailed in [Giurgiutiu 2005] and will not be repeated here. The summations in (1) cover all the symmetric (ξ^S) and antisymmetric (ξ^A) Lamb wave modes that exist for a given value of ω in a given structure. The function $\sin(\xi a)$ in (1) displays maxima when the PWAS length $2a$ equals an odd multiple of the half wavelength. Several such maxima and minima exist, each associated with a certain Lamb wave mode and its wavelength. These maxima and minima allow us to achieve Lamb mode tuning. A selected Lamb mode can be tuned by choosing the appropriate frequency for given PWAS dimensions. A plot of the strain solution in the $0 \sim 700$ kHz bandwidth for 7-mm square PWAS installed on a 1-mm thick aluminum plate is presented in Figure 2, left, while the right half of the figure gives the dispersion curves. An S0 tuning frequency can be found around 210 kHz, where the amplitude of the A0 mode is minimized while that of the S0 is still strong. In this way, we achieve tuning of the S0 mode and reject the A0 mode. Lamb wave tuning offers considerable advantages by allowing us to select the Lamb waves that are most appropriate for the particular application.

2. Lamb waves PWAS phased array design and implementation

One can employ various methods to steer and focus ultrasonic waves in certain directions. Among these methods, delay-and-sum beamforming is the oldest and simplest [Johnson and Dudgeon 1993]. The delay-and-sum beamforming was implemented in PWAS phased arrays as the embedded ultrasonic structural radar (EUSR) algorithm [Giurgiutiu et al. 2006; Yu and Giurgiutiu 2005b]. EUSR assumes that data from an M-element PWAS array is collected in a round-robin fashion by using one element at a time as transmitter and all the elements as receivers. With a total of M^2 data signals, EUSR conducts the beam scanning in virtual time as a signal post-processing operation. The EUSR beamforming and scanning procedure does not require complex devices, nor multichannel electronic circuitry as needed by the conventional ultrasonic phased array equipment. EUSR implementation of PWAS phased arrays
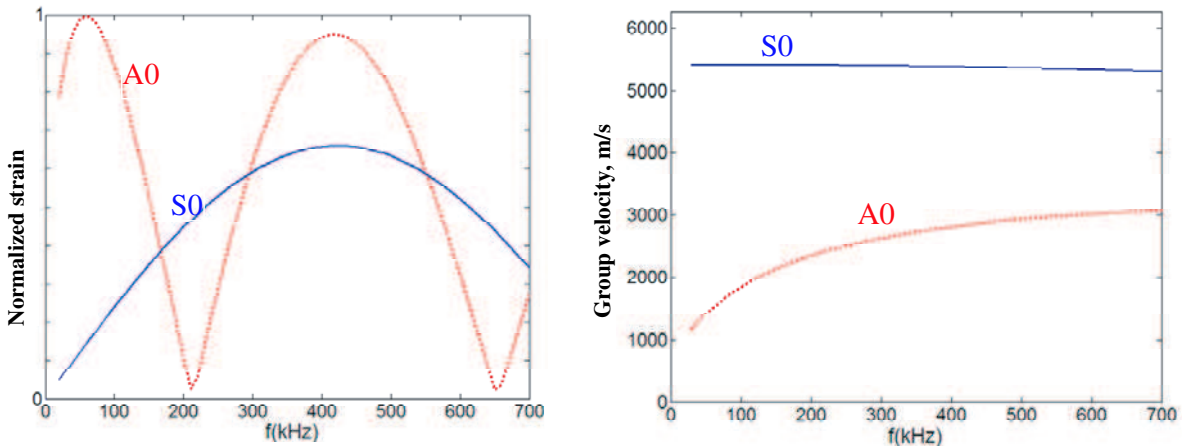
Figure 2. Lamb wave S0 mode tuning. Left: predicted Lamb wave strain curve of a 1 mm aluminum plate installed with a 7 mm square PWAS. Right: dispersion curves within $0 \sim 700$ kHz range.

requires only a function generator, an oscilloscope, a switching device, and a computer [Giurgiutiu et al. 2006].

The original EUSR algorithm uses the parallel rays approximation to simplify the beamforming calculation. This simplifying assumption is only valid if the target is far away from the phased array. If the scanning field is not sufficiently far away, the parallel ray approximation error is not negligible and the method breaks down. This can be explained as follows. When the target is not sufficiently far away from the array, that is, it is in the near field (Figure 3a), the propagating wave front is curved (circular wave front) and the wave propagating directions vary with the PWAS location. In this situation, wave propagation direction varies from PWAS element to PWAS element and individual direction vectors need to be assigned to each PWAS. Using antenna theory [Johnson and Dudgeon 1993], we define the near
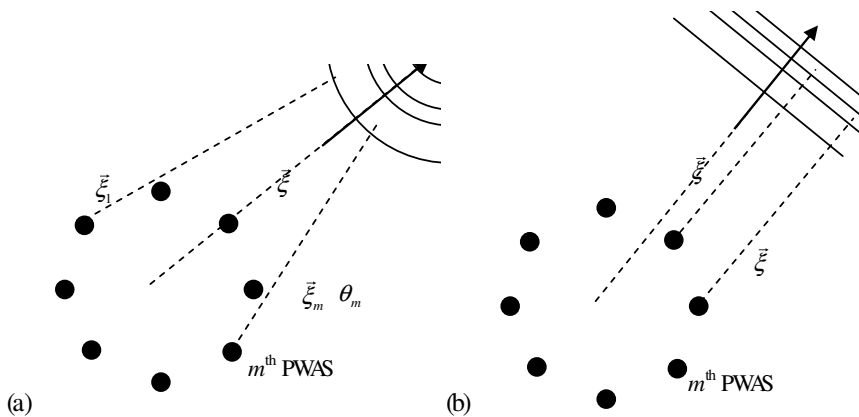

Figure 3. Wave fronts of a PWAS array: (a) near field; (b) far field.

field and far field, respectively, as the regions in which

$$0.62\sqrt{\frac{D^3}{\lambda}} < R_{\text{near}} \le \frac{2D^2}{\lambda}, \qquad R_{\text{far}} > \frac{2D^2}{\lambda}, \tag{2}$$

where D is the array aperture and λ is the excitation wavelength. Only when the target meets the far field criterion, the wave fronts are plane waves and wave propagation directions are the same for all of the array elements.

In the region $R \le 0.62\sqrt{D^3/\lambda}$, phased array theory is no longer valid; however, other methods for damage detection such as PWAS electromechanical impedance technique [Zagrai and Giurgiutiu 2001] can be employed.

2.1. *Generic beamforming formulation for PWAS Lamb waves phased arrays.* We developed generic PWAS beamforming formulas for wave beam steering at any point either in the near field or in the far field. The following assumptions are made:

- All the PWAS elements in the array lie in the same plane and behave as point-wise sources and receivers (omnidirectional);

- Monochromatic excitation and reception, without considering the dispersion of guided waves and the waves are propagating at a constant speed c in an isotropic material;

- Simultaneous excitation along the array elements.

The beamforming onto a target $P(\vec{r}, \phi)$ using an M-PWAS phased array with elements $\{\vec{s}_m\}$ is considered. The origin of coordinate system is defined in the phase center, that is, $\sum \vec{s}_m / M = 0$, for $m = 0, 1, \ldots, M-1$. For all waves arriving at the target P, the delay-and-sum beamforming consists of two steps:

(1) applying a delay Δ_m and a weighting factor w_m to the propagating wave from the m-th PWAS, $f(\vec{r}_m, t)$;

(2) summing up the output signals of the total of M PWAS.

This procedure can be expressed as

$$z(\vec{r}, t) = \sum_{m=0}^{M-1} w_m f(\vec{r}_m, t - \Delta_m).$$

For a single-tone radial wave, the wave front at a point $\vec{r}$ away from the source can be expressed as

$$f(\vec{r}, t) = \frac{A}{\sqrt{|\vec{r}|}} e^{j(\omega t - \vec{k} \cdot \vec{r})} \tag{3}$$

with $\vec{k}$ is the wave number, $\vec{k} = \vec{\xi} \cdot \omega/c$, and ω is wave frequency of the wave. For an M-element array, we apply (3) to each array element m, where $m = 0, 1, \ldots, M-1$ (see Figure 4). The m-th element is assumed at location $\vec{s}_m$, whereas the direction vector from m-th element to the target is defined as $\vec{\xi}_m$. The following notations apply

$$\vec{\xi} = \frac{\vec{r}}{r}, \quad r = |\vec{r}|, \quad \vec{k} = \vec{\xi} \cdot \frac{\omega}{c}, \qquad \vec{r}_m = \vec{r} - \vec{s}_m, \quad r_m = |\vec{r}_m|, \quad \vec{\xi}_m = \frac{\vec{r}_m}{|\vec{r}_m|}, \quad \vec{k}_m = \vec{\xi}_m \cdot \frac{\omega}{c},$$
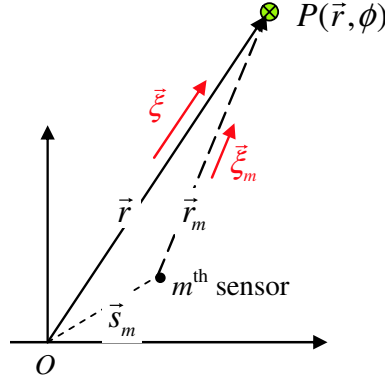
Figure 4. Schematic of the geometry of the m-th PWAS and the target at $P(\vec{r}, \phi)$.

where $\vec{k}_m$ is the wave number of the wave propagating in the direction of $\vec{\xi}_m$.

The synthetic wave front arriving at target $P(\vec{r}, \phi)$ resulting from the superposition of the waves generated by the M sources can be written as

$$z(\vec{r}, t) = \sum_{m=0}^{M-1} w_m f(\vec{r}_m, t) = \sum_{m=0}^{M-1} w_m \cdot \frac{A}{\sqrt{r_m}} e^{j[\omega t - \vec{k}_m \cdot \vec{r}_m]}. \tag{4}$$

Generic beamforming: the triangular algorithm. Equation (4) is rewritten in the form

$$z(\vec{r}, t) = f\left(t - \frac{r}{c}\right) \cdot \sum_{m=0}^{M-1} w_m \frac{1}{\sqrt{r_m/r}} e^{j\omega \frac{r-r_m}{c}}, \tag{5}$$

where the first multiplier represents the wave front emitting from a single source at the origin and is independent of the array elements. This wave is to be used as a reference for calculating the needed time delay for each elementary wave. The second multiplier is a summation which is the total effects caused by individual sources, various weighting factors and locations. Equation (5) shows that the synthetic signal $z(\vec{r}, t)$ is controlled by the multiplier

$$\sum_{m=0}^{M-1} w_m \frac{1}{\sqrt{r_m/r}} e^{j\omega \frac{r-r_m}{c}},$$

which depends on the weighting factors w_m, the location r of the target, and the locations $\vec{s}_m$ of the PWAS sources. We identify this multiplier as the *beamforming factor*, BF, given by

$$BF(w_m, r, s_m) = \sum_{m=0}^{M-1} w_m \frac{1}{\sqrt{r_m/r}} e^{j\omega \frac{r-r_m}{c}}. \tag{6}$$

Equation (6) is the direct beamforming of a group of M-PWAS fired simultaneously. To achieve beamforming in a certain direction ϕ_0, we apply certain delays to the signals from each element. The delays

are defined as $\Delta_m(\phi_0)$, $m = 0, 1, \ldots, M - 1$. Then, the beamforming formula in (6) gives

$$BF\big(w_m, r, s_m, \phi_0, \Delta_m(\phi_0)\big) = \sum_{m=0}^{M-1} w_m \frac{1}{\sqrt{r_m/r}} e^{j\omega\left(\frac{r-r_m}{c} - \Delta_m(\phi_0)\right)},$$

where r_m is a function of s_m and ϕ_0. Beamforming is achieved when the delays $\Delta_m(\phi_0)$ are chosen in such a way as to maximize BF. We observe that a maximum of $BF\big(w_m, r, s_m, \phi_0, \Delta_m(\phi_0)\big)$ is achieved if the exponential in summation equal to one, that is,

$$\frac{r - r_m}{c} - \Delta_m(\phi_0) = 0 \quad \text{(beamforming condition)}, \tag{7}$$

which yields the delays to be applied to each element:

$$\Delta_m(s_m, \phi_0) = \frac{r(\phi_0) - r_m(s_m, \phi_0)}{c}, \quad m = 0, 1, \ldots, M - 1. \tag{8}$$

Notice that the delays not only depend on the desired maximum beamforming direction, but also depend on the location of the PWAS sources. Using the delays $\Delta_m(s_m, \phi_0)$, the beamforming factor at the particular direction ϕ_0 reaches a maximum, that is,

$$BF_{\max}(w_m, r, s_m, \phi_0) = \sum_{m=0}^{M-1} w_m \frac{1}{\sqrt{r_m(s_m, \phi_0)/r}}.$$

The maximum beamforming depends on the beamforming direction ϕ_0, besides the weighting w_m, target $P(r, \phi)$, and PWAS source location s_m.

Further manipulation of the beamforming can be obtained by adjusting the weighting factors w_m. Thus far, we conclude that by applying proper time delays and weightings, the phased array beamforming at a desired direction can be achieved. When the beam steering direction ϕ_0 changes, the phased array beamforming will accomplish scanning.

Far field beamforming: the parallel algorithm. If the target meets the far field condition, the parallel ray assumption applies. The generic formulas developed in the previous section can be simplified to become independent of the target radial position. Since the propagation directions of the waves are now parallel to each other, we have

$$\vec{r}_m \parallel \vec{r}, \quad \vec{\xi}_m \approx \vec{\xi}, \quad \sqrt{r_m} \approx \sqrt{r}, \quad \vec{k}_m \approx \vec{\xi} \cdot \frac{\omega}{c} = \vec{k}, \qquad m = 0, 1, \ldots, M - 1.$$

After applying delay and weighting, the beamforming factor becomes

$$BF(w_m, \vec{s}_m, \phi_0) = \sum_{m=0}^{M-1} w_m e^{j\omega\left(\frac{\vec{\xi} \cdot \vec{s}_m}{c} - \Delta_m(\phi_0)\right)}. \tag{9}$$

For a particular direction ϕ_0, the beamforming factor can be achieved by setting $\Delta_m(\phi_0) = \vec{\xi} \cdot \vec{s}_m/c$. Substituting that into (9) gives a beamforming factor that depends only on weight w_m, that is,

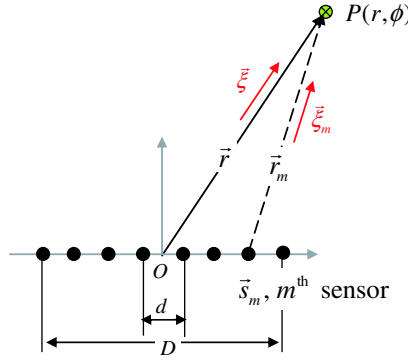$$BF \max(w_m) = \sum_{m=0}^{M-1} w_m.$$

Figure 5. Schematic of an M-PWAS phased array. The coordinate origin is located in the middle of the array.

2.2. *Directional beamforming of 1-D linear PWAS array.* The generic PWAS phased array beamforming formulas derived in the previous section will be first applied to the simplest and also one of the most practical arrays, the 1-D linear array. This is achieved by placing the PWAS along a straight line. Here, a M-PWAS linear array uniformly spaced at d is considered, as illustrated in Figure 5. The span (aperture) D of the array is $D = (M - 1) \cdot d$. With the coordinate system origin located in the middle of the array, the location vector of the m-th element and the vector r_m are

$$\vec{s}_m = \left[d\left(m - \frac{M-1}{2} \right), \, 0 \right], \qquad \vec{r}_m = \vec{r} - \vec{s}_m.$$

Recall from Equation (5) that the synthetic wave front received at $P(r, \phi)$ from the M-PWAS array is

$$z(\vec{r}, t) = f\left(t - \frac{r}{c} \right) \cdot \sum_{m=0}^{M-1} w_m \frac{1}{\sqrt{r_m/r}} e^{j\omega \frac{r - r_m}{c}}.$$

The first multiplier represents a wave emitting from the origin and it is independent of the array elements. This wave is to be used as a reference for calculating the needed time delay for each elementary wave. The second multiplier, which controls the array beamforming, can be simplified by normalizing r_m by the quantity r, resulting in the beamforming factor

$$BF(w_m, M) = \frac{1}{M} \cdot \sum_{m=0}^{M-1} w_m \frac{\exp\left(j \frac{2\pi}{\lambda} (1 - r_m) \right)}{\sqrt{r_m}}.$$

The scale factor $1/M$ is used to normalize the beamforming factor. By further introducing two new parameters, d/λ and r/d, the beamforming is rewritten as

$$BF\left(w_m, M, \frac{d}{\lambda}, \frac{r}{d} \right) = \frac{1}{M} \cdot \sum_{m=0}^{M-1} w_m \frac{\exp\left(j 2\pi \frac{d}{\lambda} \frac{r}{d} (1 - r_m) \right)}{\sqrt{r_m}}. \tag{10}$$
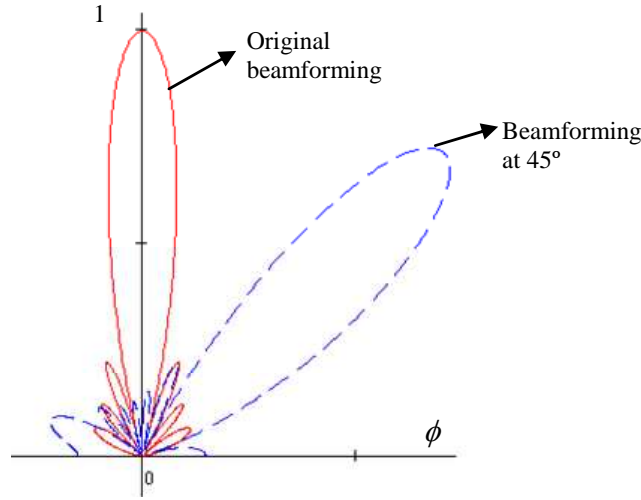
Figure 6. The original beamforming and directional beamforming at 45° of an 8 PWAS phased array with $d/\lambda = 0.5$, $r/d = 10$, $\{w_m\} = 1$.

For the far field situation, the simplified beamforming is independent of r/d, that is,

$$BF\left(w_m, M, \frac{d}{\lambda}\right) = \frac{1}{M} \cdot \sum_{m=0}^{M-1} w_m \exp\left(j2\pi \frac{d}{\lambda}\left(m - \frac{M-1}{2}\right)\cos\phi\right). \tag{11}$$

The beamforming factor in (10) and (11) has a maximum value for $\phi_0 = 90°$. This is the inherent beamforming of the linear array. The inherent beamforming for an 8-PWAS array with $\{w_m\} = 1$, $d/\lambda = 0.5$, and $r/d = 10$ is shown in Figure 6 (solid line). Notice that, indeed, the maximum beam is obtained at 90°.

Now applying "delays" $\delta_m(\phi_0)$ to steer the beam towards a preferred direction ϕ_0 the beamforming is

$$BF\left(w_m, M, \frac{d}{\lambda}, \frac{r}{d}, \phi_0\right) = \frac{1}{M} \cdot \sum_{m=0}^{M-1} w_m \frac{\exp\left(j2\pi \frac{d}{\lambda}\frac{r}{d}(1 - r_m - \delta_m(\phi_0))\right)}{\sqrt{r_m}}. \tag{12}$$

The beamforming factor of (12) reaches its maximum in direction ϕ_0 when the delay $\delta_m(\phi_0)$ is

$$\delta_m(\phi_0) = 1 - r_m(\phi_0) = 1 - \frac{|\vec{r}(\phi_0) - \vec{s}_m|}{|\vec{r}(\phi_0)|}.$$

By changing the value of ϕ_0 from 0° to 180°, we can generate a scanning beam. Simulation results of the directional beamforming at $\phi_0 = 45°$ are also shown in Figure 6.

2.3. *PWAS array implementation: embedded ultrasonic structural radar (EUSR).* The embedded ultrasonic structural radar (EUSR) methodology [Giurgiutiu and Bao 2002] was first developed under the parallel rays approximation and the assumption of a 1-D linear PWAS array permanently attached onto the structure. We generalize the original EUSR algorithm by implementing the beamforming of a generic array configuration using the exact wave propagation paths theory presented in previous sections.

For an M-PWAS array, with all elements fired simultaneously with the same excitation $s_T(t)$, the total signal arriving at target $P(r, \phi_0)$ is

$$s_P(t) = \sum_{m=0}^{M-1} w_m \frac{1}{\sqrt{r_m}} s_T \left(t - \frac{r}{c} + \frac{r - r_m}{c} \right), \tag{13}$$

where $1/\sqrt{r_m}$ represents the decay due to the omnidirectional 2-D wave radiation, r/c is the time traveling to the target from the origin O, and $(r - r_m)/c$ is the time to the target from the m-th element. Wave-energy conservation, that is, no dissipation, is assumed. If the elements are fired with certain delays rather than simultaneously, that is, $\Delta_m(\phi) = (r - r_m)/c$, Equation (13) becomes

$$s_P(t) = s_T \left(t - \frac{r}{c} \right) \sum_{m=0}^{M-1} w_m \frac{1}{\sqrt{r_m}}.$$

This shows a factor of the sum over the signal magnitude of the individual excitation $s_T(t)$.

If the delay $\Delta_m(\phi)$ is taken at $\phi = \pm\phi_0$, a maximum transmitting wave directed to the target $P(r, \phi_0)$ is thus obtained through implementing delays in the firing of the elements in the array.

After the transmission signals arrive at target P, they will be scattered and picked up by the array. The PWAS transducers serve now as receivers. The signal received at the m-th PWAS will arrive quicker by $\Delta_m(\phi) = (r - r_m)/c$. To synchronize all the received signals, we simply need to delay them with $\Delta_m(\phi) = (r - r_m)/c$. Assume that at $P(r, \phi_0)$ the incoming signal is backscattered with a backscatter coefficient A; thus, the signal received at each PWAS will be

$$\frac{1}{\sqrt{r_m}} s_T \left(t - \frac{r}{c} + \frac{r - r_m}{c} \right) A \sum_{m=0}^{M-1} w_m \frac{1}{\sqrt{r_m}}.$$

The receiver beamforming is obtained by assembling all the signals arriving at the same time, that is,

$$s_R(t) = \left(\sum_{m=0}^{M-1} w'_m \frac{1}{\sqrt{r_m}} \right) s_T \left(t - \frac{r}{c} \right) A \sum_{m=0}^{M-1} w_m \frac{1}{\sqrt{r_m}}, \tag{14}$$

where appropriate delays $\Delta_m(\phi) = (r - r_m)/c$ were used, and w'_m as the weighting for reception beamforming. Thus, the assembled received signal is further scaled by the factor $\sum_{m=0}^{M-1} w'_m/\sqrt{r_m}$.

If the location of target $P(r, \phi_0)$ is indicated by the angle ϕ_0, the coarse estimation of ϕ_0 can be implemented by using the ϕ_0 sweeping method. For linear PWAS array, the EUSR algorithm scans through $0°$ to $180°$ by incrementing ϕ_0 at $1°$ each time, and then finding the direction where the maximum received energy, max $E_R(\phi_0)$, is obtained. The received energy, $E_R(\phi_0)$ is defined as

$$E_R(\phi_0) = \int_{t_p}^{t_p + t_a} |s_R(t)|^2 dt.$$

2.4. *Proof-of-concept laboratory experiments.*
A smoothed toneburst signal of carrying frequency f_c was used to excite S0 Lamb wave mode in the PWAS array experiments. The PWAS Lamb-wave tuning principles [Giurgiutiu 2005; Bottai and Giurgiutiu 2005] were used to achieve the tuning frequency. The general form of the tone-burst excitation was $s_T(t) = s_0(t) \cos 2\pi f_c t$, where $s_0(t)$ is a short-duration
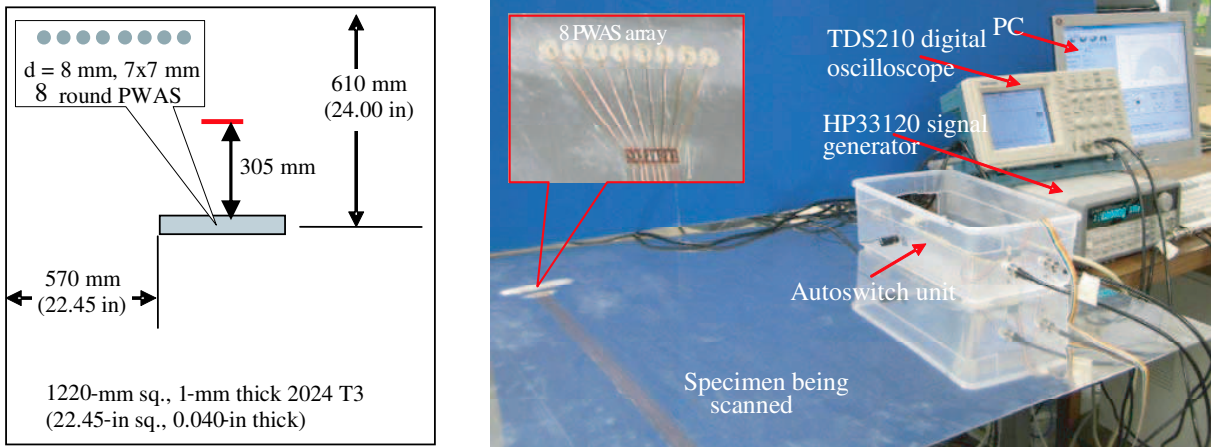
Figure 7. EUSR experiment using an 8-PWAS array: specimen layout and experiment setup.

smoothing Hanning window between 0 and t_p that is applied to the carrier signal of frequency f_c. The values t_p is calculated by $t_p = N_c/f_c$ where N_c is the count number. Since S0 is quasi-nondispersive for our fd range, we assume a constant wave speed c, and the wavelength λ was determined as $\lambda = c/f_c$.

The laboratory proof-of-concept experiments use a set of 1220 mm square 2024 T3 aluminum plates of 1 mm thickness with different damage types. A PWAS array consisting of eight 7-mm round PWAS spaced at 8 mm pitch was installed in the center of the plate, as illustrated in Figure 7, left. The damage was simulated by fully penetrated 1-mm wide and 20-mm long slits representing cracks and pin holes of various diameters. A 3-count toneburst signal was used as the excitation. The carrying frequency f_c was defined in the range $100 \sim 600$ kHz until the S0 modes was tuned at 300 kHz.

The experimental setup (Figure 7, right) includes a HP33120 function generator to send the excitation and a TDS210 digital oscilloscope to collect the signals. The collected signals were stored in a computer through the GPIB interface. A round-robin pattern was used for signal excitation and collection. At each time, one PWAS acted as transmitter to send out the excitation signal and all the PWAS served as receivers to pick up the reflection signals.

Then all the elements in the array serve as transmitters in turn. By this means, when the round-robin data collection is done, a total of M^2 signals are recorded. The switch between transmitters and receivers is implemented through the PWAS-ASCU unit described in [Liu and Giurgiutiu 2005]. A typical raw signal recorded in the experiments is shown in Figure 8. The signal-to-noise ratio for the raw signal is found to be 7.6.

The delay-and-sum beamforming procedure was processed as a post processing routine to generate a virtual scanning beam using the improved EUSR algorithm. This is advantageous and different from the traditional phased arrays instruments which have high device requirements for sending out all the phased signals simultaneously through parallel channels.

The virtual scanning result from the EUSR is visualized as a 2-D image by mapping the wave magnitude. In addition, a display of an A-scan signal at a user selected direction is also provided. Figure 9 gives an example of using the PWAS array EUSR to scan a specimen (plate #1) with a broadside crack located
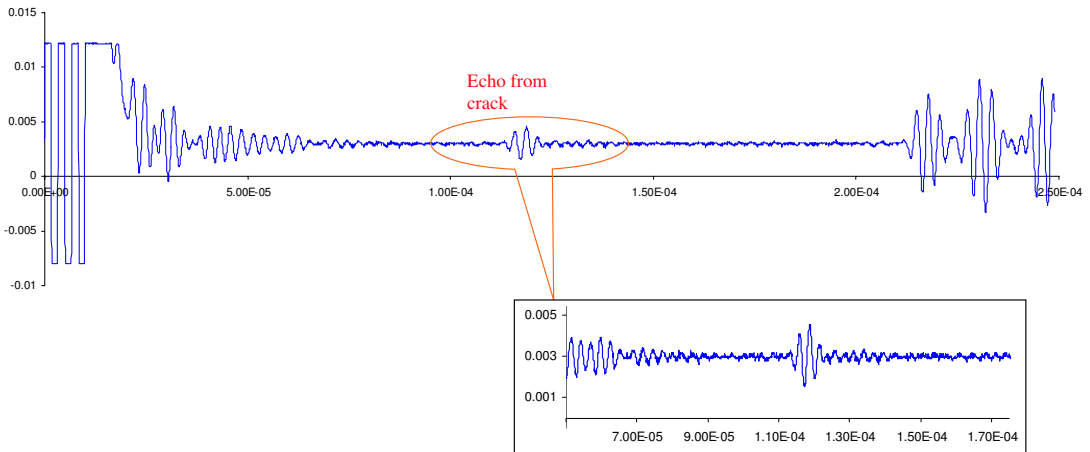
Figure 8. A typical raw signal collected in the proof-of-concept experiment with close-up plot of echo from crack.

about 305 mm in front of the array. The excitation frequency was tuned to 300 kHz where the S0 wave was dominant (Figure 9c). At this frequency, the S0 wave propagates at speed 5440 m/s with $\lambda = 18$ mm. The dark stripe seen in Figure 9b at position of 90° and about 305 mm away from the array indicated the presence of the broadside crack. Figure 9d gives the A-scan signal at 90° and 30°. Note here that an observation window is used to maximize the display by removing the initial bang and the reflections
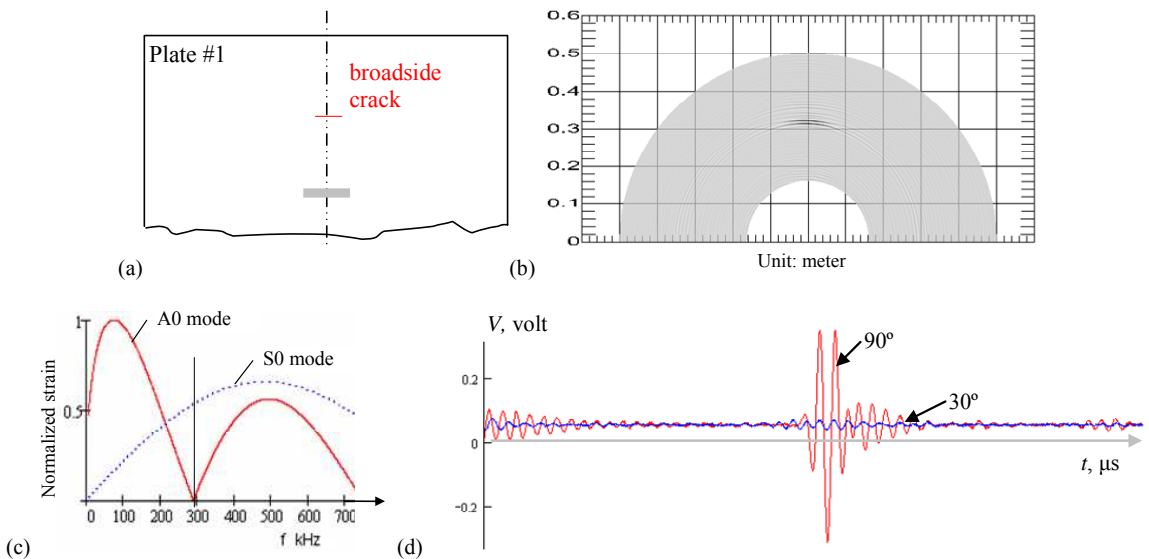

Figure 9. Proof-of-concept PWAS EUSR scanning experiment for detecting a broadside crack: (a) schematic of half a plate with a broadside crack; (b) mapped EUSR scanning image; (c) S0 mode tuning curve for using 8 mm round PWAS in a 1 mm thick aluminum plate; (d) selected A-scan at 90°.

from the boundaries. The estimated signal-to-noise ratio for the crack echo was signal-to-noise ratio of approximately 38, a great enhancement when compared with the raw signal.

The scanning image obtained from the experiment shows that EUSR can correctly show the presence of the crack and indicates that the crack is centered at 90° and around 305 mm in front of the array. These results match quite well the actual situation. However, there are a couple of dark stripes on the picture in Figure 9b and the estimation of the crack size is rather coarse. Further work was found needed to improve the image quality, as shown in the next section.

3. Advanced signal processing for EUSR

Observing the A-scan signals in Figure 9d, it is realized that the multiple lines shown in scanned image is actually caused by the multiple local maxima in the rectified signal. Such an influence can be removed by rectifying the signal and replacing it with its envelope. Moreover, background noise is present at all the time, resulting the circular ripples in the scanned image. To remove these problems, we added the Hilbert transform and thresholding to the post-processing of the EUSR system. These modules we inserted immediately after the beamforming algorithm and before the visualization section. In addition, we applied denoising and filtering at a particular frequency component using wavelet analysis and time-of-flight detection through cross correlation methods.

3.1. *Essential signal processing.* Two methods, the Hilbert transform and the thresholding process, are used as essential signal processing to enhance the EUSR image quality.

Envelop extraction using Hilbert transform. Envelope represents the absolute amplitude of a signal. It can be easily extracted through the Hilbert transform. Hilbert transform is widely used to construct an analytical signal which has the envelope of the original signal. The Hilbert transform of a signal $x(t)$ is defined as (see [Poularikas 2006, Chapter 10])

$$H(x(t)) = -\frac{1}{\pi}\int_{-\infty}^{+\infty}\frac{x(\tau)}{t-\tau}dt.$$

To build an analytical signal $\tilde{x}(t)$, the original signal $x(t)$ is employed to construct the real part, the Hilbert transform $H(x(t))$ is employed to construct the imaginary part, that is, $\tilde{x}(t) = x(t) + jH(x(t))$. The analytical signal $\tilde{x}(t)$ has the property that it has the same envelope as the original signal, that is, $|\tilde{x}(t)| = |x(t)|$. Hence we can find the envelop of the original signal $x(t)$ by taking the magnitude of the analytical signal $\tilde{x}(t)$. Figure 10 demonstrates the envelope of an A-scan signal recorded at 90° extracted with the Hilbert transform [Yu and Giurgiutiu 2005a]. The original echo of the crack shows many local maxima, which introduces difficulties in automatically detecting the location of the crack (as the case shown in Figure 9b). After extracting the envelope, there is only one peak to consider, and peak detection method can be easily applied.

Thresholding. As shown in Figure 9b, some background noise shows up in the image, resulting in the ripples in the image. To remove these ripples, a thresholding process is included after the Hilbert transform. By this means, noise signal below the threshold value will be discarded. The original and improved EUSR scanning image of the broadside crack specimen are shown in Figure 11.
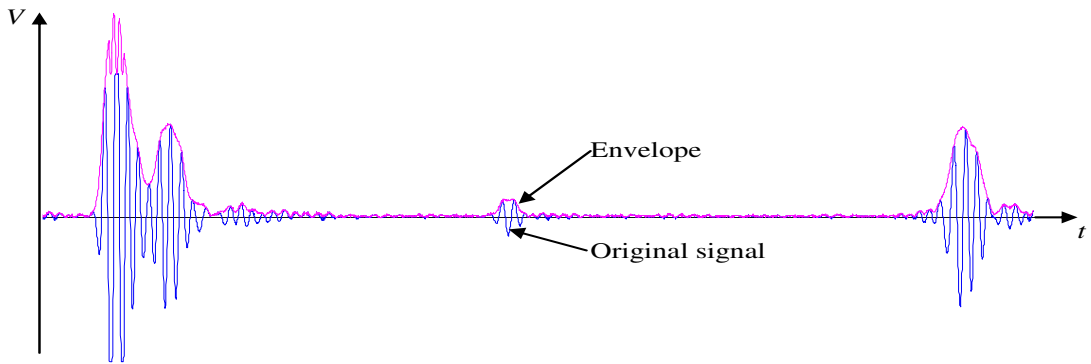
Figure 10. Envelope extraction by the Hilbert transform.

3.2. *Additional advanced signal processing.* As options, more modules have been developed for more signal processing objective as well. These modules include denoising by discrete wavelet transform, single frequency component filtering by continuous wavelet transform, and precise measurement of TOF by cross correlation method. Details of this development can be found in Yu and Giurgiutiu [2005a]. An overview is given next.

Denoising by discrete wavelet transform (DWT). Based on multiresolution analysis (MRA), the discrete Wavelet transform (DWT) provides a tool for decomposing signals into a set of elementary mutually-orthogonal building blocks, called wavelets. The DWT is defined as

$$c_{m,n} = \int_{-\infty}^{+\infty} x(t)\Psi_{m,n}(t)dt, \qquad \Psi_{m,n}(t) = 2^{-m/2}\Psi(2^{-m}t - n),$$

where $\Psi_{m,n}(t)$ are orthonormal wavelets obtained by shifting and dilating a mother wavelet $\Psi(t)$. The coefficients $c_{m,n}$ are usually considered as the result of a filter being applied to the signal; the filter is working as a highpass filter and a lowpass filter to extract the signal's approximation and detail information, respectively. After each filtering process, half of the frequencies of the original signal are removed. At the same time, half the signal samples can be discarded by a downsampling process of a factor of 2
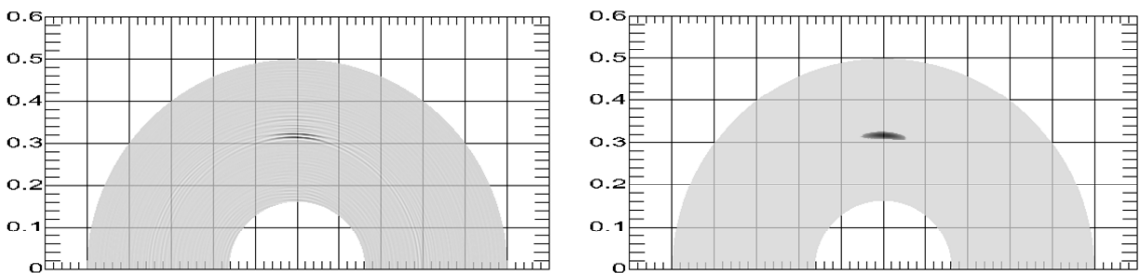

Figure 11. EUSR inspection results: original image (left) and improved image after Hilbert transform and thresholding process (right).
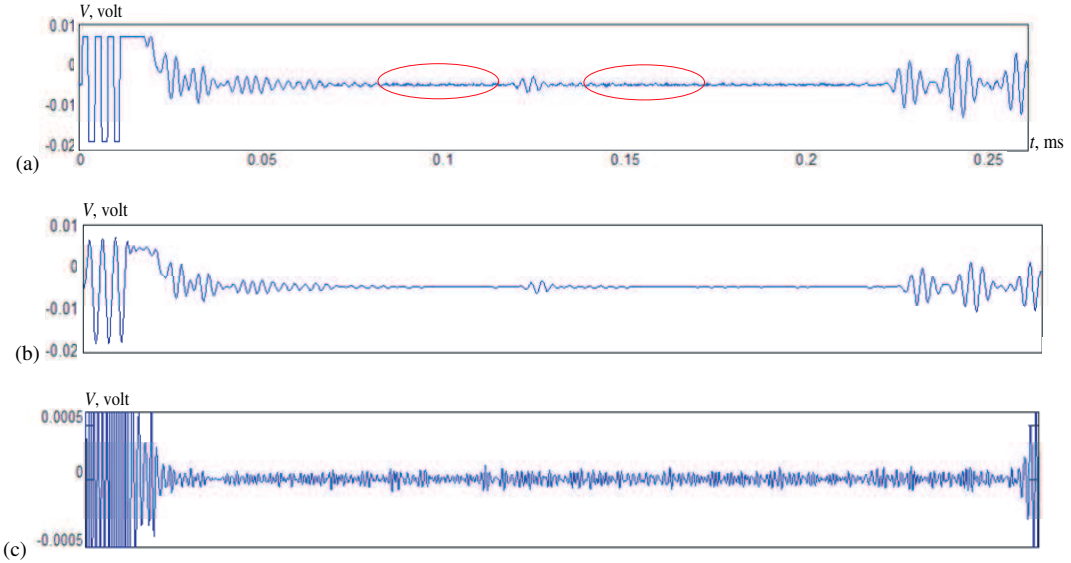
Figure 12. A 3-level DWT denoising using Mayer wavelet: (a) original signal from broadside experiment; (b) denoised clean signal; (c) removed noise.

consistent with the Nyquist rule. Such a decomposition process will continue for l times (called DWT level) until data remaining is within the user-defined allowable error range, defined in the filter bank theory [Boggess and Narcowich 2001]. Therefore, the original signal is separated into two parts, the approximation part, that is, the denoised signal, and the details part, that is, the removed noise. As an example, a raw signal recorded in the broadside experiment was processed by a 3 level DWT using the Mayer wavelet. Figure 12a shows the processed original data. Note that, in this proof-of-concept experiment, the noise level is not severe. After DWT denoising, certain noise (shown in Figure 12c at a zoomed scale) was removed and a much cleaner signal was obtained (Figure 12b). The small ripples were significantly reduced (see the circled segments between wave packets). The large components at the beginning of the noise caused by truncation in initial bang, which were not removed, but they will be later discarded through time windowing.

Filtering by continuous wavelet transform (CWT). Another way to remove disturbance is offered by the continuous wavelet transform (CWT). The CWT of signal $x(t)$ using the mother wavelet $\psi(t)$ is

$$CWT(a, \tau) = \frac{1}{\sqrt{|a|}} \int x(t) \psi^* \left(\frac{t - \tau}{a} \right) dt, \tag{15}$$

where a is the scale (or dilation) factor, τ is the translation (or time shift) of the wavelet with respect to the signal, and the factor $1/\sqrt{|a|}$ is introduced for energy normalization at different scales. The resulting scale-frequency representation of the magnitude squared, $|CWT(a, \tau)|^2$, is the scalogram

$$|CWT(a, \tau)|^2 = \frac{1}{|a|} \left| \int x(t) \psi^* \left(\frac{t - \tau}{a} \right) dt \right|^2.$$
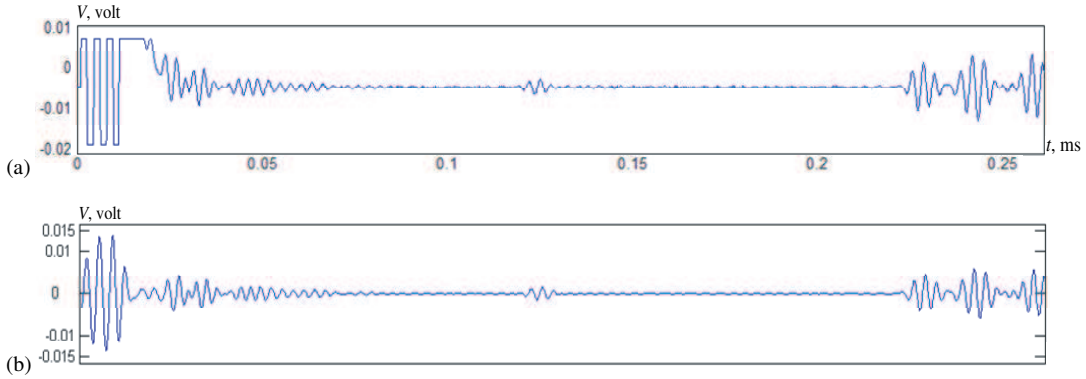
Figure 13. CWT filtering at 300 kHz using Mayer wavelet: (a) original signal; (b) CWT filtered result.

The relation between the scale and the filtering frequency f is

$$f = \frac{\text{dimensionless center frequency of the wavelet}}{(\text{scale}) \times (\text{sampling interval})}. \tag{16}$$

With Equations (15) and (16), we see that a certain frequency component of interest can be extracted by performing the CWT at the corresponding single scale. We named this process CWT filtering. In PWAS array application, though excitation at tuned frequency is employed, the signal contains multifrequency components due to tone-burst characteristics (having certain bandwidth). With CWT filtering, only the frequency component at the wavelet level corresponding to the excitation frequency is used in the reception signals, reducing the influence of spectrum spread and dispersion. By this means, disturbances from other frequencies can be removed. Figure 13 gives the filtering result of the same raw signal as used in the DWT denoising. The CWT filtering used the Mayer wavelet to extract the frequency component at 300 kHz, which is the excitation frequency. Filtered result is shown in Figure 13b. In addition to the reduced background noise, it is interesting to observe that the 300 kHz component in the initial bang was also extracted with more focused energy. This illustrates the advantage of CWT over DWT filtering.

TOF detection by cross correlation. Cross correlation is widely used to detect similarities in two signals. The cross correlation $R_{xy}(m)$ of two discrete signals $x(n)$ and $y(m)$ of length N is defined by

$$R_{xy}(m) = \frac{1}{N} \sum_{n=0}^{N-1} x(n)y(n-m).$$

When the input signal $x(n)$ slides along the time axis of the correlated signal $y(m)$ with a small step, the similarity of the overlapped part of two signals is compared. If the two signals are completely not similar (unrelated), the correlation coefficient is 0, while if they are identical, the correlation coefficient is 1. For real signals, the cross correlation method can reduce the noise since the noise is not related to the signals and not auto-related either.

In our application, since the reflection caused by the damage resembles the original excitation, its arrival time (TOF) can be extracted using the cross correlation method. Figure 14 illustrates this idea. A signal received at PWAS (Figure 14b) is correlated with the 3-count toneburst excitation (Figure 14a),
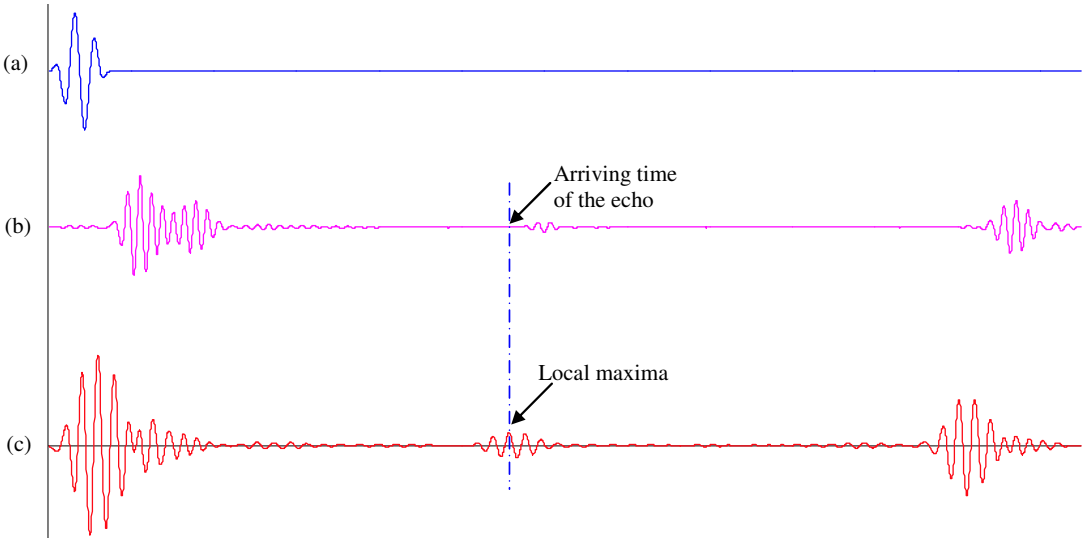
Figure 14. Cross-correlation for detecting TOF of the echo from the crack: (a) window-smoothed tone-burst excitation; (b) received signal; (c) cross-correlation coefficients of the signals.

generating a sequence of cross correlation coefficients (Figure 14c). The local maxima represent the time instants when the wave packets have largest similarity with the toneburst, that is, at the arrival time of the wave packet. To locate the TOF of echo from the crack, a time window can be used to cut off influences from the initial bang and boundary reflections. After the TOF is obtained, the location of the crack l can be estimated using the wave propagation speed c, that is, $l = c \cdot \text{TOF}$.

3.3. *Experiments with improved EUSR.* To further confirm EUSR detection ability, more experiments were conducted on different specimens. These specimens include: (1) plate #2 with a broadside crack inclined at 30°; (2) plate #3 with a horizontally positioned offside crack located at 137°; (3) plate #4 with a broadside pin hole of increasing diameter (0.5 mm, 1 mm, 1.57 mm, 2 mm); (4) plate #5 with two aligned horizontally positioned offside cracks at 67° and 117°, respectively. Specimen schematics are shown in Figure 15. All plates have the same dimension as the one used in the proof-of-concept experiment and the perpendicular distances from the damage to the array are 301 mm for all the plates.

To compare the imaging of the horizontal broadside crack specimen and the 30°-inclined crack specimen, these EUSR images are presented side-by-side in Figure 16. It is noticed that the image of the inclined crack is a little further away from the array. This is because some incipient waves were reflected away due to the slope. The inclined-crack footprint in the EUSR image is also smaller than the parallel crack. This leads to the idea of an effective crack length, $L_e = L \cos \alpha$, where $\alpha = 30°$. The slope of the crack was not clearly indicated in Figure 16, right. We believe that this is due to the lack of resolution inherent in the 300 kHz S0 Lamb wave used in the detection, which is with the crack length ($\lambda_{S0} \approx 16$ mm at 300 kHz).

The pin hole damage detection in plate #4 was started from diameter 0.5 mm and then gradually enlarged to 1 mm, 1.57 mm, and 2 mm (in accordance with available drill bit sizes). EUSR failed to
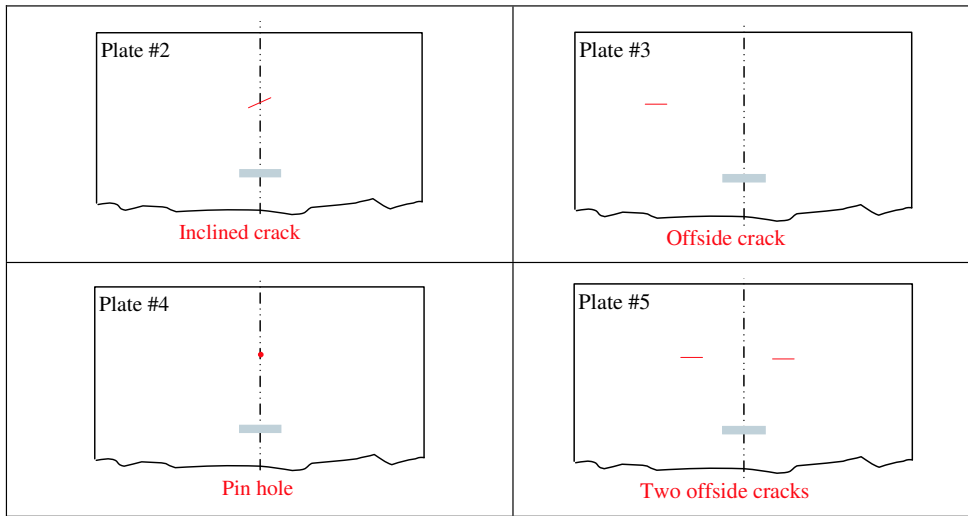
Figure 15. EUSR proof-of-concept experimental specimen schematics (all cracks are 20 mm long, 1 mm wide).

detect the pin hole of 0.5 mm diameter. Neither did it detect the pin hole of 1 mm diameter. When the hole was enlarged to 1.57 mm, EUSR gave a precise indication for the pin hole location, as shown in Figure 17, left. We considered this dimension as the minimum detectable damage dimension at this inspection frequency. The EUSR image of the 2 mm pin hole was even stronger, as shown by Figure 17, right, which is more intense than the left counterpart for the 1.57-mm pin hole.

Figure 18, left, shows the EUSR scanning image of the plate #3, which has a single offside crack at 137°. Since the crack orientation is parallel to the array alignment, most of the incipient waves are reflected away and no specular reflection is present. However, diffraction at crack tips creates sufficient back scatter waves to permit detection. The resulting EUSR image shows the presence the crack, verifying that EUSR PWAS phased array can detect cracks which are located in nonoptimal positions. The scanning of plate #5, which has two offside cracks at 67° and 117°, is shown in Figure 18, right.
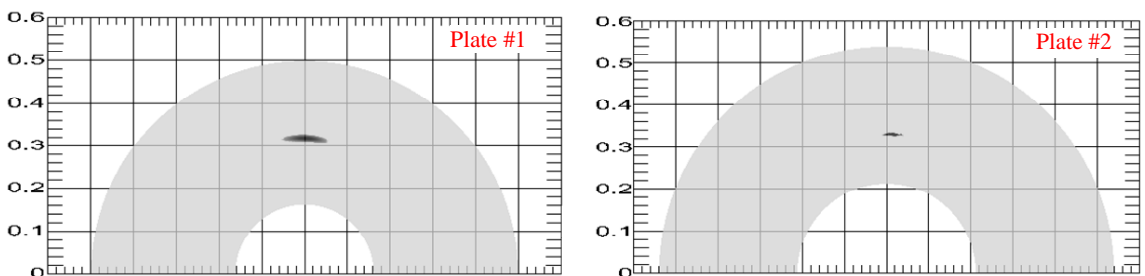

Figure 16. EUSR scanning images of the broadside crack specimens. Left: EUSR image of plate #1 with a broadside crack. Right: EUSR image of plate #2 with an inclined broadside crack.
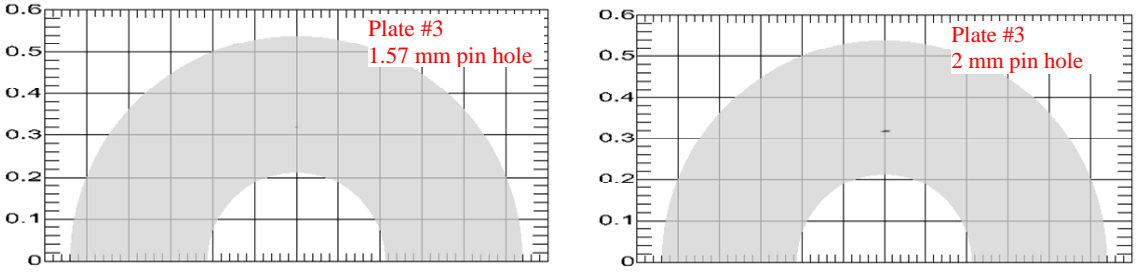
Figure 17. EUSR scanning images of the pin hole specimen. Left: EUSR image of the 1.57 mm pin hole. Right: EUSR image of the 2 mm pin hole.
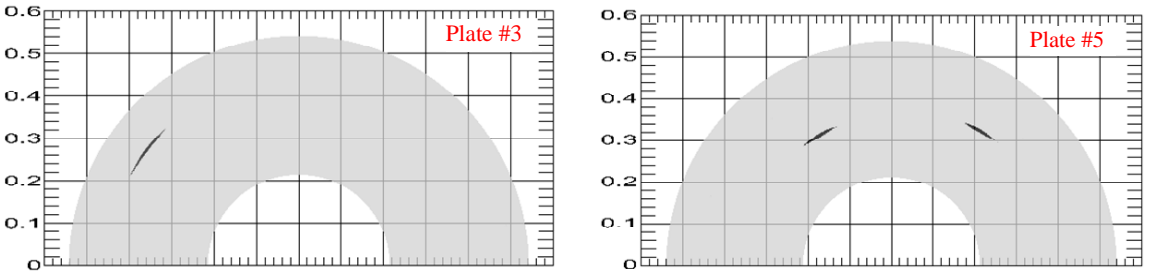

Figure 18. EUSR scanning images of the offside crack specimens. Left: EUSR image of plate #3 with an offside crack at 137°. Right; EUSR image of plate #5 with two offside cracks at 67° and 137°, respectively.

Both cracks are clearly detected in the image with correct center positions. This proves the multicrack detection capabilities of the EUSR PWAS method.

4. PWAS phased array optimization

The PWAS phased array beamforming at certain direction ϕ_0 is affected by several parameters:

- spacing between neighboring PWAS, d;
- number of PWAS, M;
- steering angle, ϕ_0;
- weighting factors, $\{w_m\}$.

Among these parameters, the effect of spacing d is always measured by the wavelength λ. Since $\lambda = c/f$, when the wavelength λ changes with the frequency, the ratio of d/λ will also change. For the triangular beamforming, there is an extra parameter needed to be considered, the ratio of r/d. Therefore, the effect of parameter d can be represented by the ratio d/λ and the ratio r/d. If all the weighting factors are the same ($\{w_m\} = $ constant), that is, all PWAS in the array are excited uniformly, this type of phased array is called uniform array. Otherwise, it is called nonuniform array. We will use the
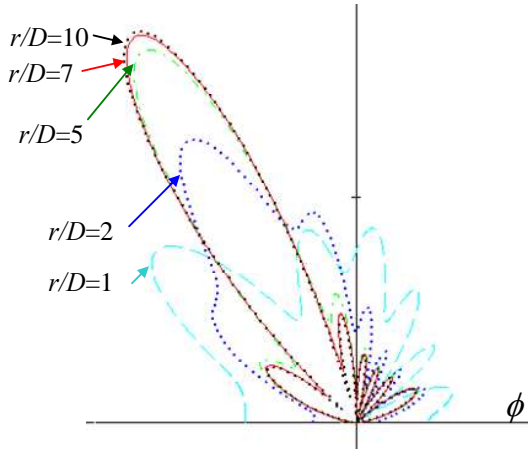
Figure 19. Beamforming at 120° of an eight PWAS phased array spacing at 0.5λ with various r/D value.

triangular beamforming algorithm to explore how these parameters affect the uniform PWAS phased array beamforming and then find out how the beamforming is modified by the weighting factors.

4.1. *Uniform PWAS phased array.* First we consider an M-element uniform PWAS array equally spaced at pitch d with equal weights, $w_m = 1$.

Effect of the r/d ratio. The ratio r/d determines whether a target is located in the far field or the near field of the phased array. If the target is in the near field, we have to use the exact triangular algorithm. Otherwise, we use the parallel ray approximation. To better quantify this ratio, the array span D is used instead of d using $D = (M - 1)d$. The field definitions of (2) can be expressed in terms of r/D

$$0.62\sqrt{(M-1)\frac{d}{\lambda}} < \left(\frac{r}{D}\right)_{\text{near}} \le 2(M-1)\frac{d}{\lambda}, \qquad \left(\frac{r}{D}\right)_{\text{far}} > 2(M-1)\frac{d}{\lambda}.$$

These definitions show that, for a particular application of an eight PWAS array spaced at half wavelength ($d = \lambda/2$), the near field is contained in the interval $r \in (1.16D, 7D]$, while the far field is the outside area ($r > 7D$). Beamforming simulations with r/D value evolving from 1, to 2, 5, 7, and 10 are shown in Figure 19 for a PWAS array directed at 120°.

The simulation used parameters from the laboratory experiments, that is, aluminum plate of 1 mm thickness and 3-count toneburst at $f_c = 300\,\text{kHz}$. Figure 19 shows that very close to the array field ($r/D = 1$), directional beamforming does no longer exist (dashed line). However, as the target moves away from the array (entering near field, $r/D = 2$), directional beamforming starts to take shape. The beamforming is getting better when far-field conditions are approached ($r/D = 5$). In far field, where parallel rays approximation applies, the effect of r/D vanishes. No significant difference can be noticed between $r/D = 7$ and $r/D = 10$.

Effect of the d/λ ratio. The ratio d/λ shows the influence of spacing on array beamforming. Simulation results of an eight PWAS array directed at 120° with various d/λ values are shown in Figure 20. By
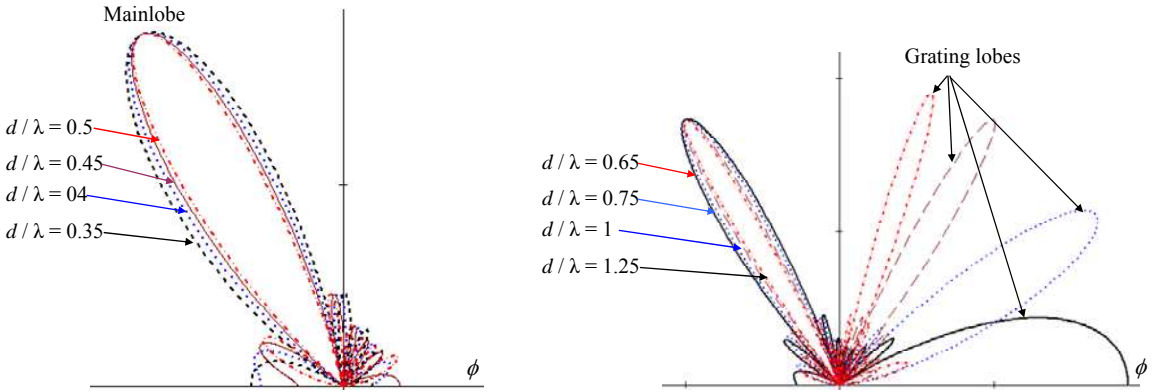
Figure 20. Beamforming at 120° of an eight-PWAS array with $r/D = 10$ using various d/λ: (a) $d/\lambda \leq 0.5$; (b) $d/\lambda > 0.5$.

comparing the beams, it can be seen that the beam width becomes smaller and smaller as d/λ increases. However, the number of sidelobes also increases. For larger d/λ value, narrow beam width (better resolution/directivity) is achieved, but more sidelobe disturbing are also presented.

It is also noticed that, for beamforming at $d/\lambda = 0.75$ and beyond (Figure 20b), besides the mainlobe at the desired angle of 120°, there are other strong and disturbing lobes showing up at other undesired directions. Such lobes are called grating lobes; they are caused by spatial aliasing [Johnson and Dudgeon 1993]. Grating lobes can have magnitudes as big as the mainlobe magnitude. The grating lobes are not desired and should be avoided because they give misleading scanning results. According to the spatial sampling theorem [Johnson and Dudgeon 1993], in order to avoid spatial aliasing, the spacing d between elements should be smaller or equal to the half wavelength ($d/\lambda \leq 0.5$). Otherwise grating lobes may appear. In practical implementation, this rule should be verified after frequency tuning. For the 300 kHz tuning frequency used in the proof-of-concept experiments, the ratio d/λ has the value $d/\lambda = 0.44$ ($d = 8$ mm; $c = 5440$ m/s). Therefore, no grating lobes are were yet presented.

Effect of the number M of PWAS in the array. The discussion about the influence of the spacing pitch on the array beamforming indicates that larger spacing may give better directional beams despite of their byproduct, larger sidelobes. However, the spacing cannot be unlimitedly increased because of the spatial sampling theorem. The number of elements in the array is another factor that affects the beamforming. Figure 21 demonstrates how beamforming is modified by different M values, for example, $M = 8$ and $M = 16$. The comparison shows the beamforming of a 16-PWAS array yields a much narrower mainlobe and slightly stronger sidelobes than that of an 8-PWAS array. Increasing the number of elements is a simple way to enhance beamforming with the small penalty of larger sidelobes. However, in practice, more elements will result in wiring issue and will be limited by the available installation space.

Effect of the steering angle ϕ_0. Steering angle ϕ_0 (beamforming direction) is another factor that affects the beamforming. Figure 22a and b shows beamforming at 0°, 30°, 60°, 90°, 120°, 150° directions using eight-PWAS and sixteen-PWAS are arrays, respectively.

An overall examination of Figure 22 indicates that the best beamforming is achieved at $\phi_0 = 90°$, with a slender and focused beam. As the angle moves to either side of the 90° position, the beamforming
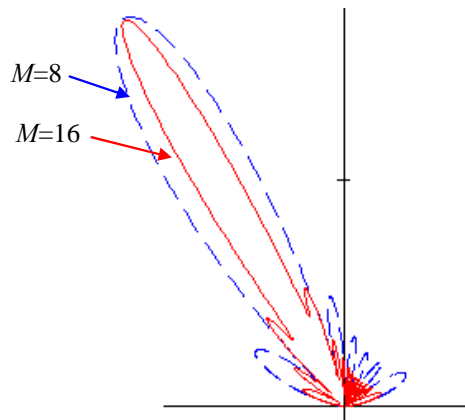
Figure 21. Beamforming at 120° of PWAS array with $r/D = 10$ and $d = 0.5\lambda$ using different M. The beam in dash is obtained with $M = 8$ and the beam in solid is obtained with $M = 16$.
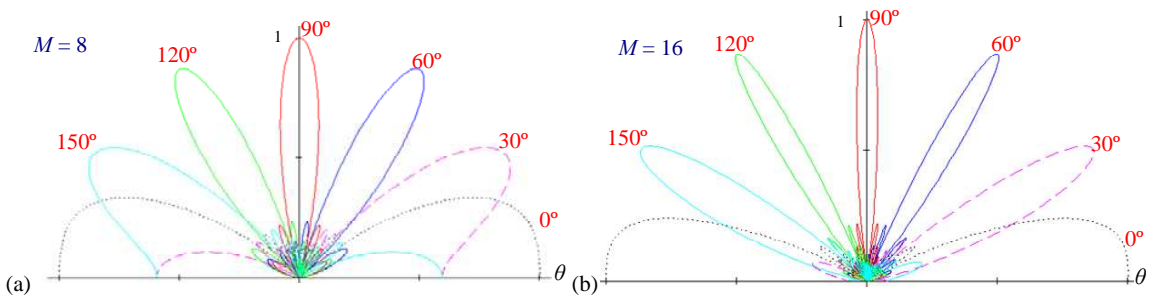

Figure 22. Beamforming at various steering angles with $D/r = 10$ and $d = 0.5\lambda$: (a) an eight PWAS array; (b) a sixteen PWAS array.

worsens. At 0° and 180°, the beamforming breaks down. In fact, at 0°, the beamforming split into two identical halves, one at 0°, the other at 180°. Such a lobe at 180° is called backlobe. As the direction increases to 30° and 60°, the back lobe shrinks and the main lobe becomes more directional. Beamforming at 120° and 150° are symmetrical about the vertical center to that at 60° and 30°. When the mainlobe gets closer to 180° (such as 150°), the back lobe starts again increasing. The directional mainlobe is completely lost again at 180°. This observations show that a linear PWAS array does not have a complete 180° view but a smaller one. The result in Figure 22b confirms the conclusion, but certain improvements due to the increased number of elements are apparent. Comparing the results for $M = 8$ to those for $M = 16$, we see that an array with larger M gives larger view area. No directional beam was obtained at 30° by the eight-PWAS array, but it was achieved by the sixteen-PWAS array.

4.2. *Nonuniform PWAS phased array.* Now we consider the case of having different excitations for the array's elements, that is, beamforming of a nonuniform PWAS array. The various excitations, if known,

can be processed as weighting factors and implemented in the EUSR algorithm, that is,

$$BF\left(w_m, M, \frac{d}{\lambda}, \frac{r}{d}, \phi_0\right) = \frac{1}{M} \cdot \sum_{m=0}^{M-1} w_m \frac{\exp\left(j2\pi \frac{d}{\lambda}\frac{r}{d}(1 - r_m - \delta_m(\phi_0))\right)}{\sqrt{r_m}}.$$

Two widely used distributions, the binomial distribution and the Dolph–Chebyshev distribution, will be used to determine the effect of relative excitation amplitudes in the array.

Binomial array. The coefficients w_m for a binomial array can be obtained by using the binomial expansion of the expression $(1+x)^M$ [Johnson and Dudgeon 1993], that is,

$$(1+x)^{M-1} = 1 + (M-1)x + \frac{(M-1)(M-2)}{2!}x^2 + \frac{(M-1)(M-2)(M-3)}{3!}x^3 + \cdots.$$

The positive coefficients of the series at different values of M serve as the relative amplitude distribution w_m for an M-PWAS array. Such a nonuniform array is thereby named a binomial array. For $M = 8$, the amplitude weights are $\{1, 7, 21, 35, 35, 21, 7, 1\}$. Beamforming simulation results for a binomial array at different d/λ values are shown in Figure 23a. Larger d/λ yields thinner mainlobe, that is, better resolution/directivity. Figure 23a also shows that the beamforming of the binomial array has no sidelobes. Actually, this is the most significant characteristic of binomial arrays. Comparison with the beamforming of an equivalent uniform array is given in Figure 23b (at $d/\lambda = 0.5$). Although the binomial array has a wider mainlobe, it has no sidelobe at all which gives stronger signal suppression in undesired directions.

The disadvantage of using binomial array becomes, however, apparent if we look at directional beamforming away from 90°, for example, $\phi_0 = 45°$. Figure 23c shows that the binomial array had already a deteriorated beamforming at 45° whereas the equivalent uniform array still has a directional beam. In addition, the zero sidelobe advantage is lost as we move away from vertical. The binomial arrays have
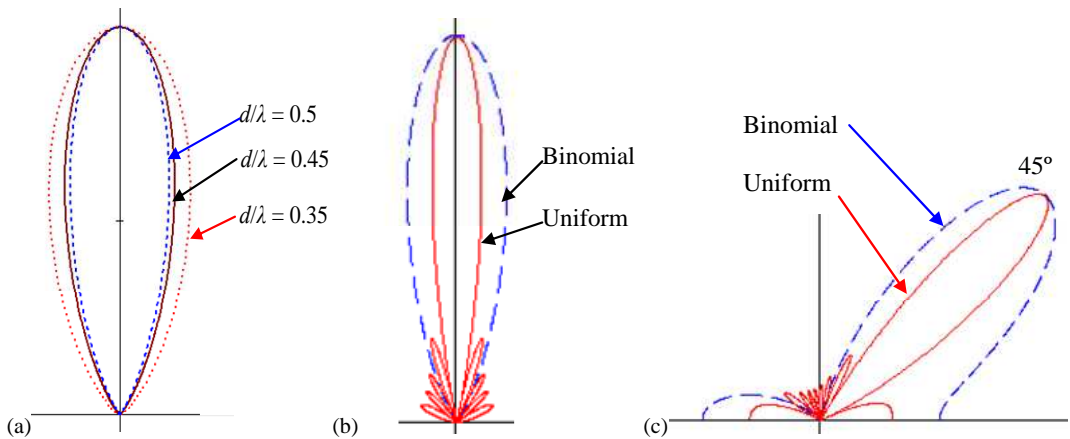

Figure 23. Beamforming of eight PWAS binomial array with $r/D = 10$: (a) beamforming at 90° of a binomial array with various d/λ values; (b) beamforming at 90° of a binomial array and an equivalent uniform array with $d/\lambda = 0.5$; (c) beamforming at 45° of a binomial and equivalent uniform array with $d/\lambda = 0.5$.
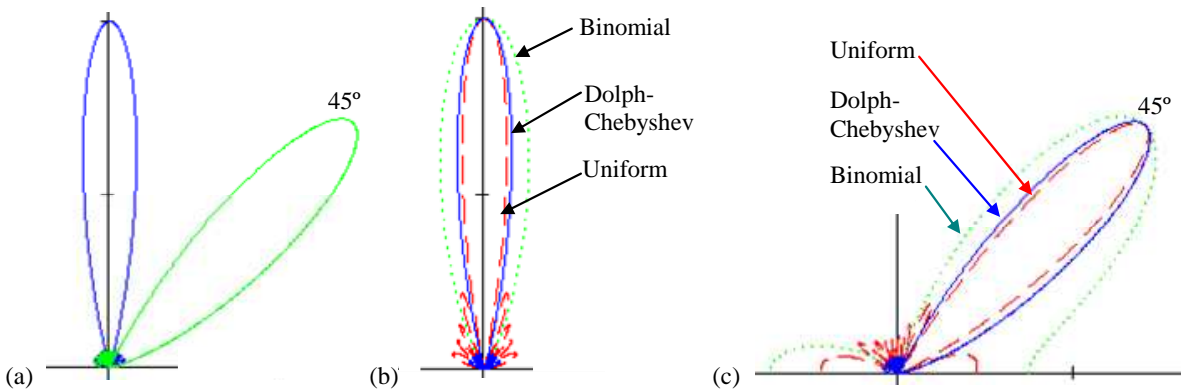
Figure 24. Beamforming of an eight PWAS Dolph-Chebyshev array with $r/D = 10$ and $d/\lambda = 0.5$: (a) beamforming at 90° and 45°; (b) beamforming at 90° of all three arrays; (c) beamforming at 45° of all three arrays.

smaller view area than the equivalent uniform arrays and sidelobes may show up when departing from front focus.

Dolph–Chebyshev array. Though binomial arrays have the unique property of zero sidelobe at 90°, they give larger beam width and smaller view area. Another feasible nonuniform array is the Dolph–Chebyshev array utilizing the Chebyshev distribution. By assigning a sidelobe level, that is, the ratio of mainlobe magnitude to the first sidelobe magnitude, the Dolph–Chebyshev array coefficients can be derived [Balanis 2005]. To build an 8-PWAS Dolph–Chebyshev array, for a desired sidelobe level of 20, the normalized coefficients w_m are given by {0.357, 0.485, 0.706, 0.89, 1, 1, 0.89, 0.706, 0.485, 0.357}. Beamforming at 90° and 45° of this Dolph–Chebyshev array with $d/\lambda = 0.5$ and $r/D = 10$ is shown in Figure 24a. It can be seen that, with the designed sidelobe level, the sidelobes are significantly suppressed. If beamforming at 90° of all the three arrays are compared (Figure 24b), we see

(1) considering the sidelobe level, the binomial array has the smallest sidelobes (zero sidelobe), followed by the Dolph–Chebyshev array while the uniform array has the highest sidelobe level;

(2) considering the mainlobe width (directionality), the uniform array has the thinnest mainlobe and the Dolph–Chebyshev array is slightly larger, with the binomial array of largest width.

Beamforming at 45° is shown in Figure 24c. At this direction, the Dolph–Chebyshev array still has low sidelobes and directional beamforming. In summary, the Dolph–Chebyshev array is a good compromise between sidelobe level and mainlobe width. While sidelobes are suppressed, its directivity at off angles is still well maintained.

4.3. *Experiments with weighted EUSR for nonuniform arrays.* The simulation results presented in the previous section have shown that the Dolph–Chebyshev array is expected to have much smaller sidelobes when compared to the equivalent uniform array, while having almost the same mainlobe width. For the binomial array, it is expected to have much smaller sidelobe level but with enlarged mainlobe width. Using the experimental data from the broadside crack specimen collected with the 8-PWAS uniform
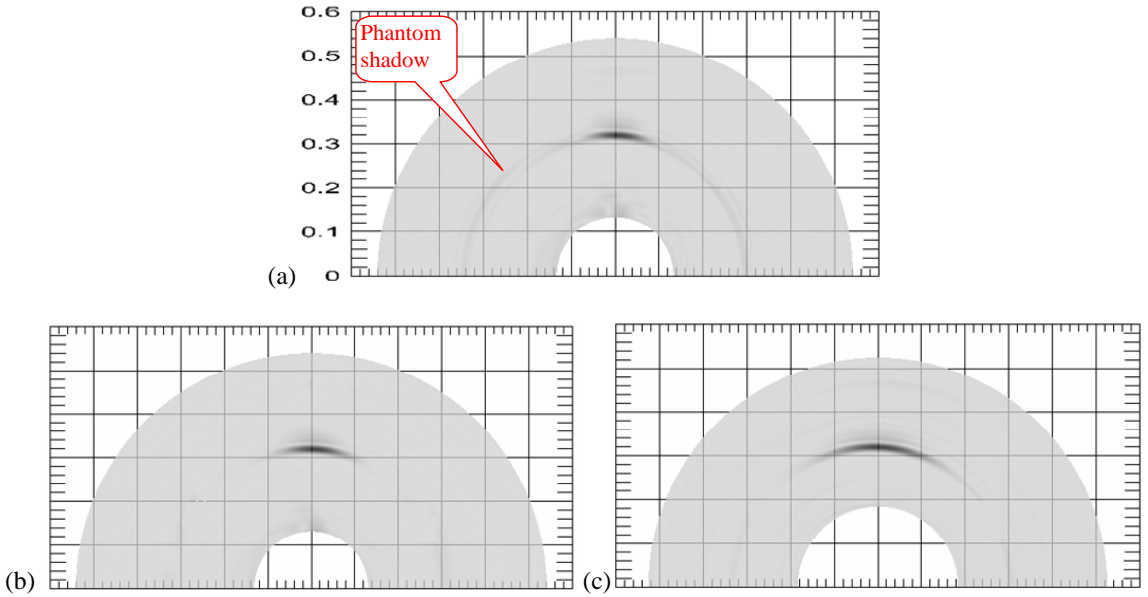
Figure 25. Crack detection using weighted EUSR algorithms on eight PWAS nonuni-
form arrays: (a) image of the original uniform array; (b) image of the Dolph–Chebyshev
array; (c) image of the binomial array.

array, we implemented the nonuniform arrays with the weighted EUSR algorithm. Figure 25a gives
the uniform array's EUSR image before thresholding process. A phantom shadow is present as a ring
in which the crack shows up. Recalling the beamforming simulation results in Figure 24b, we know
that this is caused by the sidelobe effect. With either the Dolph–Chebyshev array or the binomial array,
the corresponding weighted EUSR algorithm should give better images with the phantom removed or
reduced. The scanning results of the two nonuniform arrays are shown in Figure 25b and Figure 25c,
respectively.

Immediately we observe that the sidelobe phantom has been sufficiently suppressed in both images,
as expected. But the crack size in the binomial array image is much wider than that of the uniform array.
The wider crack image further verifies that the binomial array produces the largest mainlobe width among
the three array considered in this study.

5. Conclusions

In this paper, we presented new developments of a novel SHM method, the embedded ultrasonic structural
radar (EUSR) [Giurgiutiu et al. 2006]. The EUSR method uses piezoelectric wafer active sensors (PWAS)
phased array to create directional Lamb wave for systematically interrogating large areas of a thin-wall
structure. After a brief presentation of using PWAS transducers to send and receive Lamb waves, we
introduced the frequency tuning technique that enables the application of phased array theory to PWAS
coupled Lamb waves.

Original EUSR algorithm was developed on the parallel rays approximation in order to simplify the beamforming calculation. However, the simplifying assumption is only valid when the target is far away from the phased array and if the scanning field is not sufficiently far away, the method will deteriorate. To overcome this problem, a generic beamforming formula, called triangular algorithm, was developed by using exact wave traveling path for the calculation. Research results show that by applying proper time delays and weightings, the phased array beamforming at a desired direction can be achieved through this generic algorithm.

To verify the damage detection ability of PWAS phased array algorithm, a set of laboratory experiments using a linear 8-PWAS array were conducted to detect various damages in aluminum plates. The beamforming is implemented as the signal post-processing algorithm, known as the EUSR method. This post processing approach used in PWAS phase array implementation is advantageous over the conventional ultrasonic phased arrays methods since sophisticated multichannel electronic devices are not needed to precisely delay the individual signals going to the phased array elements. EUSR system collects data in a round-robin fashion, then performs the scanning in virtual time, and presents the result as a 2-D image. A proof-of-concept experiment was conducted and successfully verified the crack detection ability of the EUSR approach.

To improve the display image quality, several advanced signal processing methods were discussed for current or potential applications in EUSR routine. Signal preprocessing methods include the DWT denoising to remove the noise and CWT f_c-component filtering to eliminate the influence resulted from spectrum spreading and Lamb waves dispersion. The signal post-processing after EUSR algorithm includes two steps. First Hilbert transform is used to extract the A-scan signal envelope thus avoiding the ambiguity caused by multiple local peaks. Then the thresholding process is applied to remove the background noise. Thus, a clear image with sharp contrast can be obtained to indicate the presence of damage in the structure with better precision. To locate the position of the crack, TOF detection module using the cross-correlation method was also implemented. Several experiments were conducted to estimate the detection ability of the EUSR algorithm.

Beamforming properties of linear PWAS array were investigated. We found that several parameters can be used to manipulate the output beamforming. They are: ratio d/λ, ratio r/d, number of elements M, steering angle ϕ_0, and weighting factors w_m. The effects are concluded as following:

- Larger d/λ results in thinner mainlobe width. However, the requirement of $d/\lambda \leq 0.5$ should be met to observe the spatial sampling theorem. Otherwise, grating lobes are present.

- Larger r/d ratio results in better beamforming for the triangular algorithm.

- Larger M results in thinner mainlobe though the sidelobe level gets larger which wiring may become an issue.

- The effective viewable area of linear arrays is less than 180°. The actual range is affected by number of elements and weighting.

- Weighting can further modify the beamforming, affecting, the mainlobe width, the sidelobes, and viewable area.

Experimentally, two types of nonuniform PWAS arrays were implemented, the Dolph–Chebyshev array and the binomial array. This was done by using a weighted EUSR algorithm. The results coincide

with the simulation results: (1) in terms of mainlobe width, uniform array is the best, followed by the Dolph–Chebyshev array while the binomial array yields the largest mainlobe; (2) in terms of sidelobes, the binomial array can achieve the "no sidelobe" effect at 90° when spaced at half wavelength, while the Dolph–Chebyshev array has manipulated sidelobe levels.

In a summary, the original contributions of this paper can be summarized as follows:

1. The paper presents an exact beamforming formulation using the exact wave traveling path rather than using the conventional parallel ray approximation.

2. The paper explores how the PWAS phased array beamforming is affected by several phased array parameters.

3. The paper presents how advanced signal processing methods can be used to improve the PWAS phased array performance.

4. The paper verifies the potential application of nonuniform PWAS phased array in the pattern of binomial array and Dolph–Chebyshev array.

Using proof-of-concept experiments, we have shown that the PWAS phased arrays implemented with the EUSR algorithm has great potential for in-situ structural health monitoring. To apply this technique to structures with complicated geometries or to detect small targets (weak reflectors) etc., more research needs to be done. The use of the generic PWAS array beamforming formulas can be applied to 2-D array configurations to obtain full range 360° scanning. Sustained theoretical research and technological development will continue to be conducted to more this technique toward practical SHM implementation.

References

[Balanis 2005] C. A. Balanis, *Antenna theory analysis and design*, Wiley, Hoboken, NJ, 2005.

[Beral and Speckmann 2003] B. Beral and H. Speckmann, "Structural health monitoring (SHM) for aircraft structures: a challenge for system developers and aircraft manufacturers", pp. 12–29 in *Proceedings of Structural Health Monitoring 2003: From diagnostics and prognostics to structural health monitoring* (Stanford, CA), edited by F.-K. Chang, Destech, Lancaster, PA, 2003.

[Boggess and Narcowich 2001] A. Boggess and F. Narcowich, *A first course in wavelets with Fourier analysis*, Prentice-Hall, Upper Saddle River, NJ, 2001.

[Bottai and Giurgiutiu 2005] G. Bottai and V. Giurgiutiu, "Simulation of the lamb wave interaction between piezoelectric wafer active sensors and host structure", pp. 259–270 in *Smart structures and materials 2005: sensors and smart structures technologies for civil, mechanical, and aerospace systems* (San Diego), edited by M. Tomizuka, Proceedings of SPIE **5765**, SPIE, Bellingham, WA, 2005.

[Giurgiutiu 2005] V. Giurgiutiu, "Tuned lamb wave excitation and detection with piezoelectric wafer active sensors for structural health monitoring", *J. Intell. Mater. Syst. Struct.* **16**:4 (2005), 291–306.

[Giurgiutiu and Bao 2002] V. Giurgiutiu and J. Bao, "Embedded-ultrasonics structural radar for the nondestructive evaluation of thin-wall structures", pp. paper # 2002–39017 in *Proceedings of the 2002 ASME International Mechanical Engineering Congress and Exposition* (New Orleans), ASME, New York, 2002.

[Giurgiutiu and Yu 2006] V. Giurgiutiu and L. Yu, "Optimized embedded ultrasonics structural radar (EUSR) with piezoelectric wafer active sensors (PWAS) phased arrays for in-situ wide-area damage detection during SHM and NDE", invention disclosure submitted to USC-USCRF, June 2006.

[Giurgiutiu and Zagrai 2000] V. Giurgiutiu and A. Zagrai, "Characterization of piezoelectric wafer active sensors", *J. Intell. Mater. Syst. Struct.* **11** (2000), 959–976.

[Giurgiutiu et al. 2006] V. Giurgiutiu, J. Bao, and A. N. Zagrai, "Structural health monitoring system utilizing guided Lamb waves embedded ultrasonic structural radar", US Patent No. US6996480B2, Feb. 7 2006.

[Johnson and Dudgeon 1993] D. H. Johnson and D. E. Dudgeon, *Array signal processing: concepts and techniques*, Prentice-Hall, Upper Saddle River, NJ, 1993.

[Krautkramer and Krautkramer 1990] J. Krautkramer and H. Krautkramer, *Ultrasonic testing of materials*, vol. Berlin, 4th rev. ed., Springer, 1990.

[Liu and Giurgiutiu 2005] W. Liu and V. Giurgiutiu, "Automation of data collection for PWAS-based structural health monitoring", pp. 1139–1147 in *Smart structures and materials 2005: sensors and smart structures technologies for civil, mechanical, and aerospace systems*, edited by M. Tomizuka, Proceedings of SPIE **5765**, SPIE, Bellingham, WA, 2005.

[Moles et al. 2005] M. Moles, N. Dube, S. Labbe, and E. Ginzel, "Review of ultrasonic phased arrays for pressure vessel and pipeline", *J. Pressure Vessel Technol.* **127**:3 (2005), 351–356.

[Poularikas 2006] A. D. Poularikas (ed.), *The transforms and applications handbook*, CRC Press, Boca Raton, FL, 2006.

[Rose 1995] J. L. Rose, "Recent advances in guided wave NDE", pp. 761–770 in *1995 IEEE ultrasonics symposium*, 1995.

[Rose 1999] J. L. Rose, *Ultrasonic waves in solid media*, Cambridge University Press, 1999.

[Rose 2001] J. L. Rose, "A vision of ultrasonic guided wave inspection potential", pp. 1–5 in *Proceeding of the 7th ASME NDE topical conference*, NDE Topical Conference **20**, 2001.

[Viktorov 1967] I. A. Viktorov, *Rayleigh and Lamb waves: physical theory and applications*, Plenum Press, New York, 1967.

[Yu and Giurgiutiu 2005a] L. Yu and V. Giurgiutiu, "Advanced signal processing for enhanced damage detection with embedded ultrasonics structural radar using piezoelectric wafer active sensors", *Smart Struct. Syst.* **1**:2 (2005), 185–215.

[Yu and Giurgiutiu 2005b] L. Yu and V. Giurgiutiu, "Improvement of damage detection with the embedded ultrasonics structural radar for structural health monitoring", pp. 1081–1090 in *Proceedings of Structural Health Monitoring 2005: Advances and challenges for implementation* (Stanford, CA), edited by F.-K. Chang, Destech, Lancaster, PA, 2005.

[Zagrai and Giurgiutiu 2001] A. Zagrai and V. Giurgiutiu, "Electro-mechanical impedance method for crack detection in thin plates", *J. Intell. Mater. Syst. Struct.* **12**:10 (2001), 709–718.

LINGYU YU: yu3@engr.sc.edu
Department of Mechanical Engineering, University of South Carolina, Columbia, SC 29208, United States

VICTOR GIURGIUTIU: giurgiut@engr.sc.edu
Department of Mechanical Engineering, University of South Carolina, Columbia, SC 29208, United States